HydroResearch 8 (2025) 139–151

Contents lists available at ScienceDirect

HydroResearch

journal homepage: http://www.keaipublishing.com/en/journals/hydroresearch/

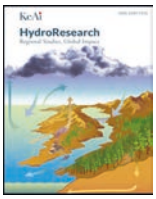

Riverine flood hazard map prediction by neural networks

Zeda Yin *, Arturo S. Leon

Department of Civil and Environmental Engineering, College of Engineering and Computing, Florida International University, Miami, FL, USA

ARTICLE INFO

Article history:
Received 20 June 2024
Received in revised form 25 October 2024
Accepted 26 October 2024
Available online 28 October 2024

Keywords:
Deep learning
Flood map prediction
Boundary conditions to image

ABSTRACT

Severe flooding can pose significant risks to human lives, result in substantial economic losses, and contribute to environmental problems such as soil salinization. An accurate early flood prediction system can effectively minimize these losses. Numerical method was the dominant approach for predicting flood inundation maps in the past decades. However, high-fidelity two-dimensional numerical methods are typically time-consuming. Machine learning methods have gained popularity in recent years, but generating a flood map directly with a small sample of boundary conditions remains challenging and largely unexplored. In this paper, we have developed a machine learning framework capable of directly predicting the maximum flood inundation map from boundary conditions. In our model, time-series boundary conditions are embedded into a higher-dimensional shape and then processed by a transformer encoder. The feature maps, post-processed by the transformer encoder, will be coupled with geophysical information such as a digital elevation map and Manning's coefficient map before being passed to the U-Net structure to obtain the final results. Our proposed model demonstrated notably high accuracy when tested with historical hurricane events. The mean absolute error of our proposed method on all test sets is 0.00717 ft., and the root mean squared error is 0.03974 ft. Furthermore, we conducted parametric studies on the model architecture and observed that they are not as sensitive as input features. Lastly, we provided explanations on why some certain geophysical features are necessary to accurately predict flood inundation maps in this paper.

1. Introduction

Floods are not only one of the most frequent natural disasters (Parhi, 2018), but they also cause more annual damage than any other weather-related natural hazards in the United States (NOAA, 2016). Between 1998 and 2017, flood events affected two billion people in some reports (Cred, 2018). Extreme floods not only endanger human lives (Haltas et al., 2021) but also result in substantial economic losses and environmental issues (Gu et al., 2022; Chen et al., 2023). For example, Hurricane Harvey led to economic losses exceeding $125 billion in 2017 (Kousky et al., 2020). In July 2021, Henan, China, experienced a record-breaking rainstorm that claimed 398 lives and resulted in an economic setback of $17.8 billion (He et al., 2023). More recently, in August 2023, Typhoon Doksuri struck northeast China, causing a severe flood that displaced over a million people. Also in November 2021, an atmospheric river brought unprecedented heavy rainfall to parts of southern British Columbia in Canada and northwestern Washington State in the United States, leading to a historic and tragic flooding event. As global warming intensifies hydrological cycles, there is a growing number of reports of unprecedented flooding worldwide in the past five years (Bevacqua et al., 2019; Kam et al., 2021). Many recent studies suggest that global warming will result in more destructive flooding events in the near future (Gu et al., 2022; Voosen, 2022). Therefore, the development of early flood warning systems and flood emergency evacuation plans is becoming increasingly significant and urgent to preserve lives and minimize economic damage. Since these decision-making systems typically rely on the outputs of flood prediction models, the accuracy and speed of these flood prediction models become critical.

As of now, numerical hydrodynamic models remain the mainstream approach in engineering for forecasting two-dimensional flood hazard maps. Prominent and widely used hydrodynamic models, such as HEC-RAS (USACE, 2018), FLO-2D (FLO-2D, 2018), and SRH-2D (Lai, 2010), are developed to numerically solve the two-dimensional shallow water equations. Numerous researchers have widely employed these models to simulate various flood scenarios across different floodplains in the past years (Ongdas et al., 2020; Pathan et al., 2022; Shaikh et al., 2023). Even though the accuracy and reliability of the numerical method has been widely verified, conducting high-fidelity two-dimensional hydrodynamic simulations remains a time-consuming task (He et al., 2023). In terms of emergency evacuation, every second matters as shorter decision-making time could save more lives and reduce the associated economic losses. In terms of optimal flood control,

* Corresponding author.
E-mail address: zyin005@fiu.edu (Z. Yin).

https://doi.org/10.1016/j.hydres.2024.10.003

Nomenclature

Abbreviation	Definition
SWEs	shallow water equations
H	water surface elevation
h	water depth
q	flux term (e.g. lateral flow flux)
t	time
u	horizontal direction velocity in Cartesian directions
v	vertical direction velocity in Cartesian directions
g	acceleration due to gravity
ν_t	eddy viscosity
c_f	bottom friction coefficient
f	Coriolis parameter
BC	boundary conditions
DEM	digital elevation model
x	horizontal direction in Cartesian directions
y	vertical direction in Cartesian directions
D	surface's smoothness dimensionless constant
n	spatial Manning's coefficient
GIS	Geographic Information System
MLP	multi-layer perceptron
CNN	convolutional neural network
RNN	recurrent neural network
GRU	gated recurrent unit
LSTM	long short-term memory
MAE	mean absolute error
RMSE	root mean square error

using numerical model as predictive model (or response surface, or environment) is very time-consuming because it needs to be executed over thousands of times to obtain the optimal sequences. Using numerical methods as predictive models will make the entire optimization process impractical, as it would take over several days. Thus, to keep balance between accuracy and the total computational time is very challenging for numerical methods.

With rise of artificial intelligence in recent years, deep learning models have shown remarkable successes in many hydrology and hydraulic fields (Hosseiny et al., 2020; Tamiru and Dinka, 2021; Park et al., 2022; Shi et al., 2023; Yin et al., 2023). A number of previous studies have explored the prediction of maximum water depth or stage during flood events using a variety of machine learning models, including MLP/ANN (Berkhahn et al., 2019; Hosseiny et al., 2020; Kim and Han, 2020; Xie et al., 2021), RNN/GRU/LSTM (Pan et al., 2020; Yan et al., 2023; Zhou and Kang, 2023), CNN/U-Net (Kabir et al., 2020; Hosseiny, 2021), and Conv-RNN/LSTM (Ha et al., 2021; Shi et al., 2023).

However, most of these models (e.g. MLP and RNN-based model) are more suitable on predicting water depth or water stage at one or several observation points rather than entire flood map in a 2D domain (Tehrany et al., 2019; Kabir et al., 2021; Rahman et al., 2021). Even latest studies are still trying to simplify the problem to predict the flood information on pre-selected sample points instead of entire map (Rahman et al., 2021; Amiri et al., 2024; Fereshtehpour et al., 2024; Hitouri et al., 2024). Due to the 2D nature of flood hazard map, the number of output variables (pixels or cells in a map) is way more than the input variables (time- series boundary conditions). Another challenge that hinders the effectiveness of deep learning models in predicting 2D flood inundation maps from boundary conditions is the nature of the models themselves. The previously mentioned MLP/ANN, RNN/GRU/LSTM, Conv-RNN/LSTM models were initially designed for sequence processes, such as time series forecasting, rather than working with 2D maps. Even though CNN/U-Net was designed for image processing, it can only accept input data being in a 2D image format. In our problem, boundary conditions in riverine systems typically do not provide sufficient information for inputting into the CNN/U-Net model. Thus, using machine learning models to directly predict flood inundation map without any impractical assumptions remains very challenging. As a result, there is still a very limited number of previous studies that have utilized deep learning models to predict 2D flood inundation maps (Bentivoglio et al., 2022).

To address these challenges, many pervious researches tried to predict the flood inundation or hazard map in an indirect way or downsize the problem complexity. For instance, some earlier studies tried to convert the flood water depth prediction problem to a classification task (Bui et al., 2020). They utilized Geographic Information System (GIS) digital elevation data to estimate the probability of flooding for individual cells or pixels (Bui et al., 2020; Nemni et al., 2020; Muñoz et al., 2021). While this approach could offer a solution by simplifying numerical value of output into Boolean value, it also reduces the level of information to the engineers, operators, and other practitioners. Another recently developed approach to rapidly generate high-resolution flood maps by using super-resolution techniques (Fraehr et al., 2023; He et al., 2023; Yin et al., 2024). This method employs neural networks to learn the relationship between high-resolution simulation results and low-resolution results, enabling the rapid transformation of low-resolution simulations into high-resolution flood inundation maps. However, this method still needs to take the advantage of low-fidelity numerical models. One pervious study initially partitioned the entire domain into several small areas or patches. Then, they used the neural networks to infer the flood conditions in other unknown areas based on the information of flood known areas. (Löwe et al., 2021). Lastly, a number of previous studies have attempted to forecast 2D flood maps using a set of machine learning models or neural networks (Esfandiari et al., 2020; Farhadi and Najafzadeh, 2021; Seydi et al., 2022; Liao et al., 2023). In these approaches, a single machine learning model or neural network is typically employed to learn and predict a small distinct sub-area, and then ensemble together into a large complete 2D map. Even though this ensemble method can partially solve the challenge, two main problems persist. Firstly, as each sub-area is independently modeled, the output features may turn out discontinuous at the interfaces connecting these sub-areas. Secondly, the number of required machine learning models is contingent on the study area, making it challenging to generalize the model across different regions. Therefore, despite considerable efforts in previous studies, the direct prediction of water depth and extent across a desired area only based on boundary conditions remains blank. To fill this research gap, this paper introduces a single-model approach capable of predicting flood maps exclusively through the utilization of boundary conditions.

Considering in the recent advancement of deep learning technology in computer vision, a few text-to-image frameworks have made remarkable strides by leveraging Transformer based models (e.g. vision Transformer, Swin Transformer) (Ding et al., 2021; Dou et al., 2022; Chang et al., 2023) and Diffusion models (Saharia et al., 2022; Ruiz et al., 2023). These models exhibit impressive generative capabilities and have the potential to greatly assist our task. However, simply adapt the method into water resources filed is still challenging. One reason is that these models are typically trained on large public image datasets, such as COCO, JFT-300 M or CIFAR-10, which often contain between 1 and 300 million training examples. Collecting such a large dataset for training these advanced models is infeasible for our flood map prediction problem. To overcome this issue, we proposed a novel framework that combines a Transformer encoder and a U-Net architecture as a decoder. Through this proposed method, our framework can take the advantages of both a large generative model and a small image model, enabling the generation of flood maps with high accuracy while using a smaller training dataset. Furthermore, the proposed method allows us to incorporate geophysical information, such as elevation, slope, Manning's coefficient, and more, into the neural networks.

This geophysical information can help the neural networks in achieving high accuracy and rapid convergence.

Direct predicting flood hazard map from only boundary conditions is highly challenging and has not been achieved by previous research. The major objective of this paper is to introduce a novel method capable of achieving this goal. The main contributions of this paper are listed as follows:

- We proposed a novel framework that can directly predict flood hazard map by incorporating geophysical information and boundary conditions. This method does not require massive training data, and it can work accurately with very small training dataset.
- This framework employs relative and position embedding to transform time-series data into a 2D map format. It then utilizes a transformer encoder to enhance the model's generative capability. Finally, the information is integrated with geophysical data in the U-net architecture to ensure accuracy when training data is limited.
- We evaluated the model's performance across four historical flood events and conducted a study of the model architecture to validate our hypothesis.

2. Methodology

2.1. Overview of mathematics in our neural network model

The riverine flood problem is governed by two-dimensional shallow water equations (SWEs), which can be derived from Navier-Stokes equations after a few assumptions (Martínez-Aranda et al., 2022). 2D SWEs consist of the mass conservation equation, the x-direction momentum equation, and the y-direction momentum equation, which is shown in Eq. 1 to Eq. 3 respectively.

$$\frac{\partial H}{\partial t}+\frac{\partial (hu)}{\partial x}+\frac{\partial (hv)}{\partial y}+q=0 \tag{1}$$

$$\frac{\partial u}{\partial t}+u\frac{\partial u}{\partial x}+v\frac{\partial u}{\partial y}=-g\frac{\partial H}{\partial x}+\nu_t\left(\frac{\partial^2 u}{\partial x^2}+\frac{\partial^2 u}{\partial y^2}\right)-c_f u+fv \tag{2}$$

$$\frac{\partial v}{\partial t}+u\frac{\partial v}{\partial x}+v\frac{\partial v}{\partial y}=-g\frac{\partial H}{\partial y}+\nu_t\left(\frac{\partial^2 v}{\partial x^2}+\frac{\partial^2 v}{\partial y^2}\right)-c_f v+fu \tag{3}$$

where H stands for the water surface elevation, h represents the water depth, q is a flux term, t is time, u and v represent velocity in Cartesian directions, g represents acceleration due to gravity, ν_t denotes the eddy viscosity, c_f represents the bottom friction coefficient, and f denotes the Coriolis parameter.

The water surface elevation and the water depth at each pixel or cell can be mutually converted if the elevation information for those pixels or cells is available. As a result, our neural network model is anticipated to have three output variables: h, u, v. For the input side, adding boundary conditions is also mandatory because the shallow water equation itself is a partial differential equation (PDE). If the boundary conditions are uncertain, it can lead to an infinite number of solutions. Consequently, the 2D Shallow Water Equations (SWEs) can be summarized in Eq. 4.

$$[h,u,v]=\mathcal{F}(t,x,y,q,\nu_t,c_f,f,BC,DEM) \tag{4}$$

where *BC* represents boundary conditions, and *DEM* represents digital elevation model.

In deep learning framework, the temporal variable, t, can be replaced by an initial positional embedding process (Liu et al., 2021), and the 2D image's position naturally represents the spatial variables: x and y. Thus, both the temporal and spatial index variables can be eliminated from the input variable list before entering the neural network. The flux term, q, is usually neglected in most cases by assuming no infiltration or evaporation because that is less important in riverine flooding compared to inland flooding. Also, to better convey our main objective and idea, we decided not to complicate the demonstration case too much. The turbulence viscosity term in the hydrodynamic model is typically calculated by using an empirical equation that involves a dimensionless constant: D. This dimensionless constant, D, is determined by the surface's smoothness and is commonly presented as spatial information, which could be added as an additional feature map at the start of the U-Net. However, in this study, we have omitted the consideration of turbulence effects because they only become significantly influential in large-scale coastal regions. The bottom friction, c_f, is usually determined by Manning's coefficient, n, which is a spatial geophysical parameter. The Coriolis parameter, f, can be directly calculated based on the latitude. Since latitude maintains a fixed linear relationship with the spatial variable, y, when the computational domain stays same, the coefficient can be safely neglected in the regression models. On the output side, all outputs depend solely on the input variables rather than on other output variables. Moreover, the water depth at peak time is a subset of the spatiotemporal set of h. As a result, we can further simplify the 2D Shallow Water Equations (SWEs) into a final approximate form, presented as Eq. 5.

$$[h_m]\cong\mathcal{F}(BC,DEM,n) \tag{5}$$

where h_m stands for the water depth at maximum flood inundation area, n represents the spatial Manning's coefficient.

2.2. Neural network model architecture

Three input variables, *BC*, *DEM*, and n, differ in dimensionality. The *DEM*, and n, are spatial data, whereas *BC* is spatiotemporal data. Therefore, it is necessary to employ different neural network architectures to handle them separately to achieve maximum performance. An overview of the proposed framework is shown in Fig. 1.

Our proposed method processes the flow hydrograph and water stage hydrograph separately, given their distinct properties. The initial step in our method involves embedding the hydrographs with positional information and reshaping them into a spatial format that matches the dimensions of *DEM* and n. The details of reshaping and positional embedding can be found in original vision transformer paper (Dosovitskiy et al., 2020) and our open-source code in Open Research section. Then, a standard vision transformer encoder process is employed to further extract deep features from the hydrographs. The details of the vision transformer encoder process could refer to the original paper (Dosovitskiy et al., 2020). In this study, the transformer encoder is executed in three steps: linear projection, adaptive positional embedding, and the transformer itself. Linear projection divides the entire feature map into smaller patches: 16×16. Adaptive positional embedding step is to add a set of learnable parameters on each patch to retain the positional information, as the subsequent MLP network does not naturally contain positional information. The detailed illustration of the self-attention mechanism in transformer encoder is shown on the left in Fig. 2. The transformer encoder, following the architecture of Vaswani et al. (2017), consists of alternating layers of multi-head self-attention and MLP block. Differ from original transformer encoder, we observed that achieving better performance in this study can be done without employing residual connections after the multi-head self-attention layer and without introducing layer normalization before the MLP block. We hypothesize that many well-known large models typically have very deep encoder structures, often consisting of 8 to 12 layers. In such cases, short residual connections can be beneficial in mitigating gradient vanishing. However, in our experiments, where the encoder layers were not as deep in most test scenarios, omitting residual connections yielded better results. It's also worth noting that reintroducing residual connections and applying layer normalization

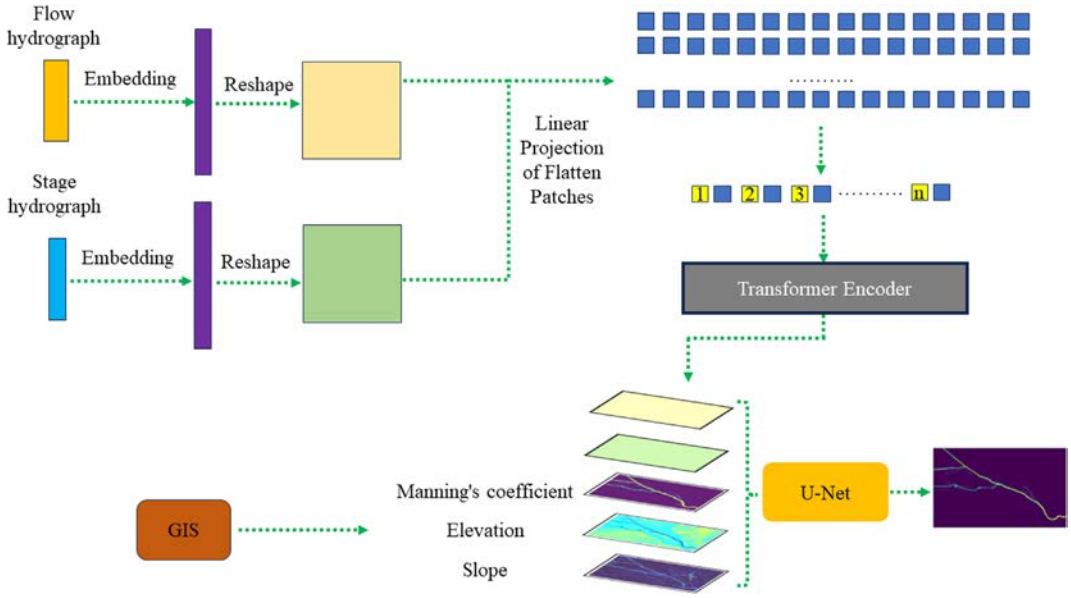

Fig. 1. Overview of the proposed method.

could improve performance in other case studies. We encourage further research to test and verify this hypothesis, especially in water resource engineering application domain. Technically, vision transformers utilize every pixel for embedding on every medium-sized image patch (Dosovitskiy et al., 2020). However, this method requires significant memory capacity and long computation time (Liu et al., 2021). To address this issue, we employed an embedding switch mechanism, as detailed in a recent study by Liu et al. (2023). The illustration of the embedding switch method is shown on the right side in Fig. 2. This method computes attention in horizontal and vertical directions in turns, effectively reducing the required GPU memory.

Once the transformer encoder step is completed, the small patches will be reassembled into a complete feature map. The feature maps of the flow and stage hydrographs are then concatenated with spatial geophysical information in the channel dimension and input into the U-Net (Ronneberger et al., 2015). An overview of the U-Net architecture is illustrated in Fig. 3. The U-Net architecture consists of three core elements: the contracting path on the left side, the expansive path on the right side, and skip connections between the contracting and expansive paths. Throughout this process, the model can extract more comprehensive, higher-level features and reconstruct full-resolution segmentations based on these higher-level features. In this paper, we employ the Res-U-Net structure, which incorporates residual blocks to provide the alternative information flow to address the issue of gradient vanishing (He et al., 2016). Due to GPU memory constraints, a small batch size is utilized in this study, therefore, we removed the batch normalization process inside the ResBlock.

3. Case study

3.1. Study area

The Miami River originates in the Everglades and flows through Downtown Miami before joining with the Biscayne Bay in the south

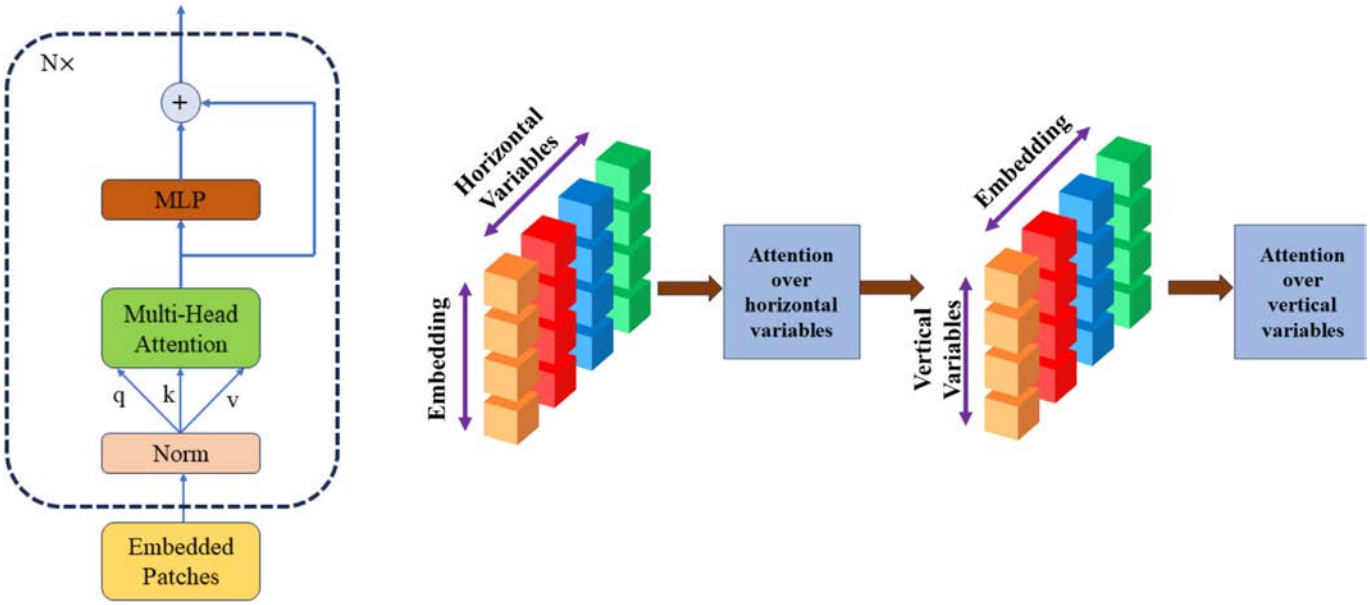

Fig. 2. The illustration of transformer encoder in our proposed method: (left) self-attention mechanism; (right) embedding switch mechanism.

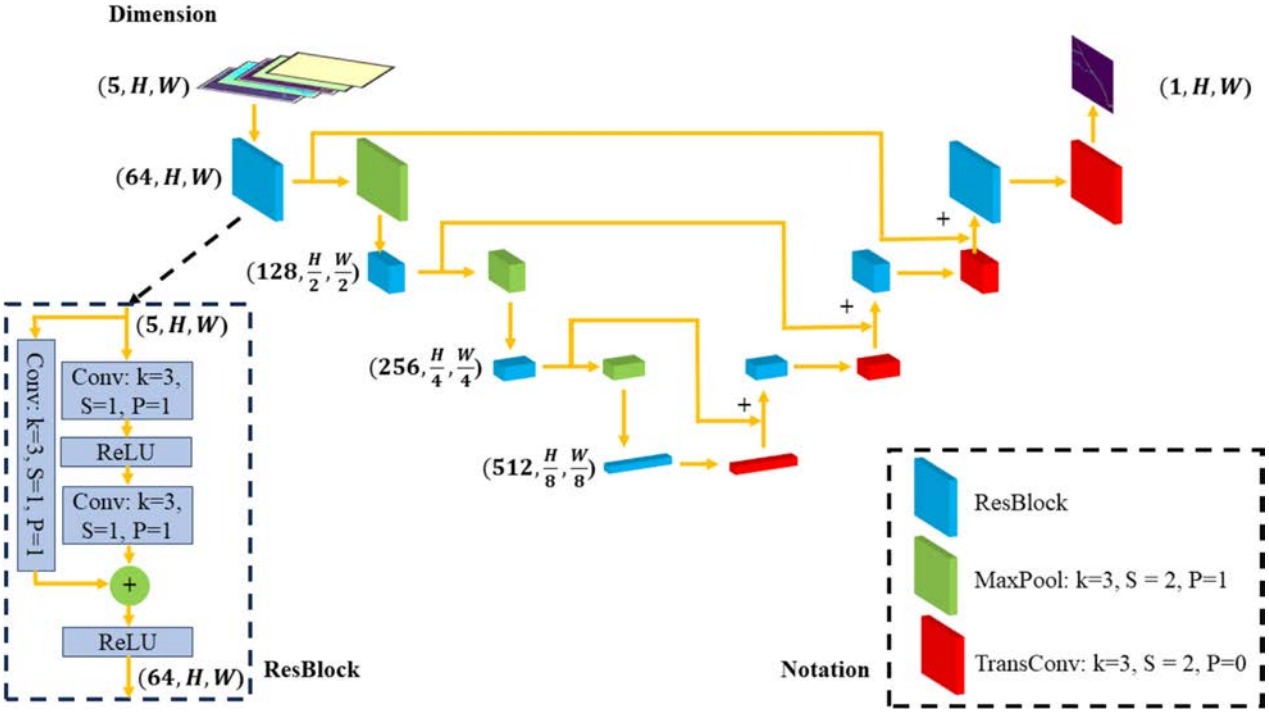

Fig. 3. U-Net structure.

Florida. A large number of residential areas, businesses and industries sit along the river and its tributaries, resulting in a densely populated urban waterway network. This study area, located in the coastal zone, is susceptible to severe hurricanes events with heavy rainfall and flooding (Azzi et al., 2020). Given its substantial economic significance, dense population, and heightened vulnerability to hurricane impacts, it serves as an ideal case study for this paper. Fig. 4 shows the location of the study area.

Fig. 5 shows the elevation layout of the study area. The elevation data is derived from the digital elevation model (DEM), crafted by the Florida Geographic Information Office. Within our study area, highlighted within the red box, elevations range from −2 ft to 40 ft. Bathymetric data is sourced from the South Florida Water Management District (SFWMD). Our study area contains 5.6 miles of the downstream Miami River and two tributaries: C4 (upper) and C6 (lower). Five water monitoring stations, marked by red triangles, are located at the boundary of our study area. These stations serve as both boundary conditions and validation points for our numerical model.

Upstream water stations, namely S25A, S25B, and S26, have various hydraulic structures, including spillway gates, culverts, and pumps.

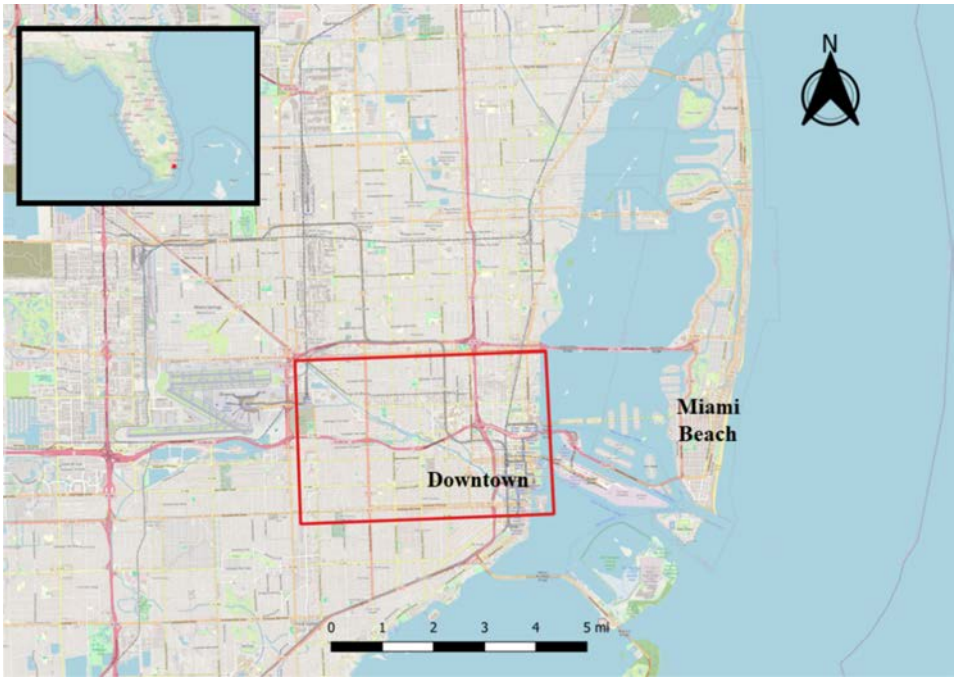

Fig. 4. Geographic map of downstream Miami River.

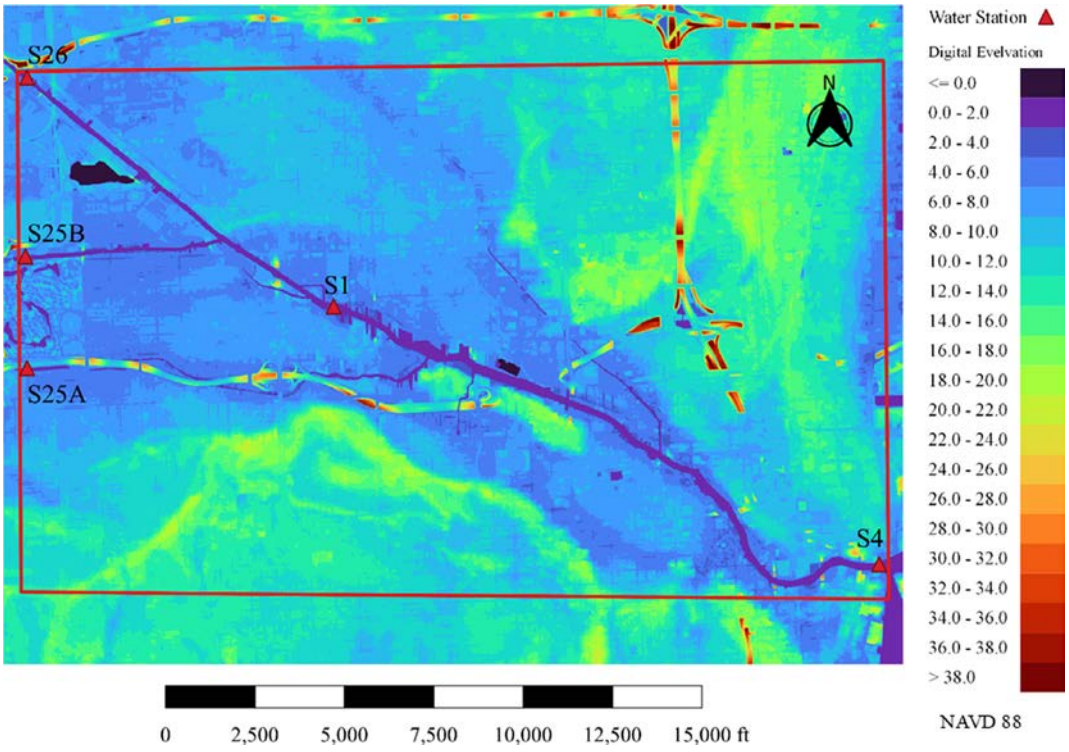

Fig. 5. Schematics and elevation information of the study area.

Flow data regulated by these structures is recorded at three-minute intervals and is employed as boundary conditions in our HEC-RAS model. The water station S4, records the downstream tide information, which is used as downstream stage boundary conditions in this study. Furthermore, water station S1, located at the center of the study area, is used for recording water stage data, which serves as a validation point for our HEC-RAS model. Our HEC-RAS model exhibited Mean Absolute Error ranging from 0.065 to 0.087 ft., and Root mean square error ranging from 0.142 to 0.182 ft. across three validation events.

3.2. Data preparation

The training dataset for our proposed method can be collected either from historical observations, such as satellite maps during flood events, or from numerical models. In practice, using historical observations for training typically provides better prediction performance. However, for demonstration purposes, all the training and test data utilized in this study are generated by a numerical model: HEC-RAS. The mesh size used in this study is 40 ft, and a full momentum equation solver is used due to study domain is influenced by the tidal conditions. The 7-day unsteady event are simulated at both training and test dataset. The original boundary condition data were obtained from DBHYDRO, provided by the South Florida Water Management District (SFWMD). The training data spans a 25-year period from 1990 to 2015. However, due to the low frequency of flood events during these 25 years, the collected training dataset is insufficient for training purposes. Therefore, we augmented the existing historical data by adding noise, generated from a Gaussian distribution, to create additional training data. In total, we have 41 sets of training data. In this study, four test scenarios were employed: Hurricane Irma from 2017, Tropical Storm Isaias from 2020, Hurricane Ian from 2022, and an amplified Hurricane Ian. The amplified Hurricane Ian is a hypothetical scenario created by doubling the flow rate and increasing downstream stage by 1 ft at each time step under Hurricane Ian condition.

4. Results

4.1. Prediction results and visualization

The predicted and simulated water depth under different hurricane events is shown in Fig. 6. The background map represents elevation data, and the water depth is visualized using a Black-Blue linear scheme after clipping values below 0.1 ft. As Fig. 6 shows, our method demonstrates strong performance, accurately predicting the majority of inundated areas in both intense flooding and non-flooding scenarios. Notably, our proposed method can successfully capture the intricate details of flood depths at the street level, making it feasible to identify which streets are affected by flooding.

The prediction error maps for four test events are shown in Fig. 7. The prediction error is computed by subtracting the predicted values from the simulated values at each pixel or cell. As Fig. 7 shows, the prediction results from our proposed method exhibit good accuracy, with the majority of pixels falling within a range of −0.5 to 0.5 ft. However, our proposed method may lead to overestimation and underestimation at a pair neighboring pixel. This indicates that predicted water surface elevation might not exhibit the ideal smooth surface as numerical results from computational physical models. For the test cases involving overland flooding, the maximum prediction errors for overland flood depths are typically greater than those for the river channel. However, it's important to note that these significant prediction errors are limited to specific small areas.

In Fig. 8, we present the predicted water depths alongside the simulated water depths in the main river channel. Our proposed method generally exhibits a tendency to very slightly underestimate the water depth of the main channel in three out of four test scenarios. Notably, the prediction errors remain relatively small for real historical events, same as the prediction of overland flood depths as shown in Fig. 7. However, these errors tend to increase during the last hypothetical amplified test event. This could be attributed to two possible reasons. Firstly, it is possible that the manipulated amplified boundary conditions do not align with the natural patterns in the history record, making it challenging for the model to

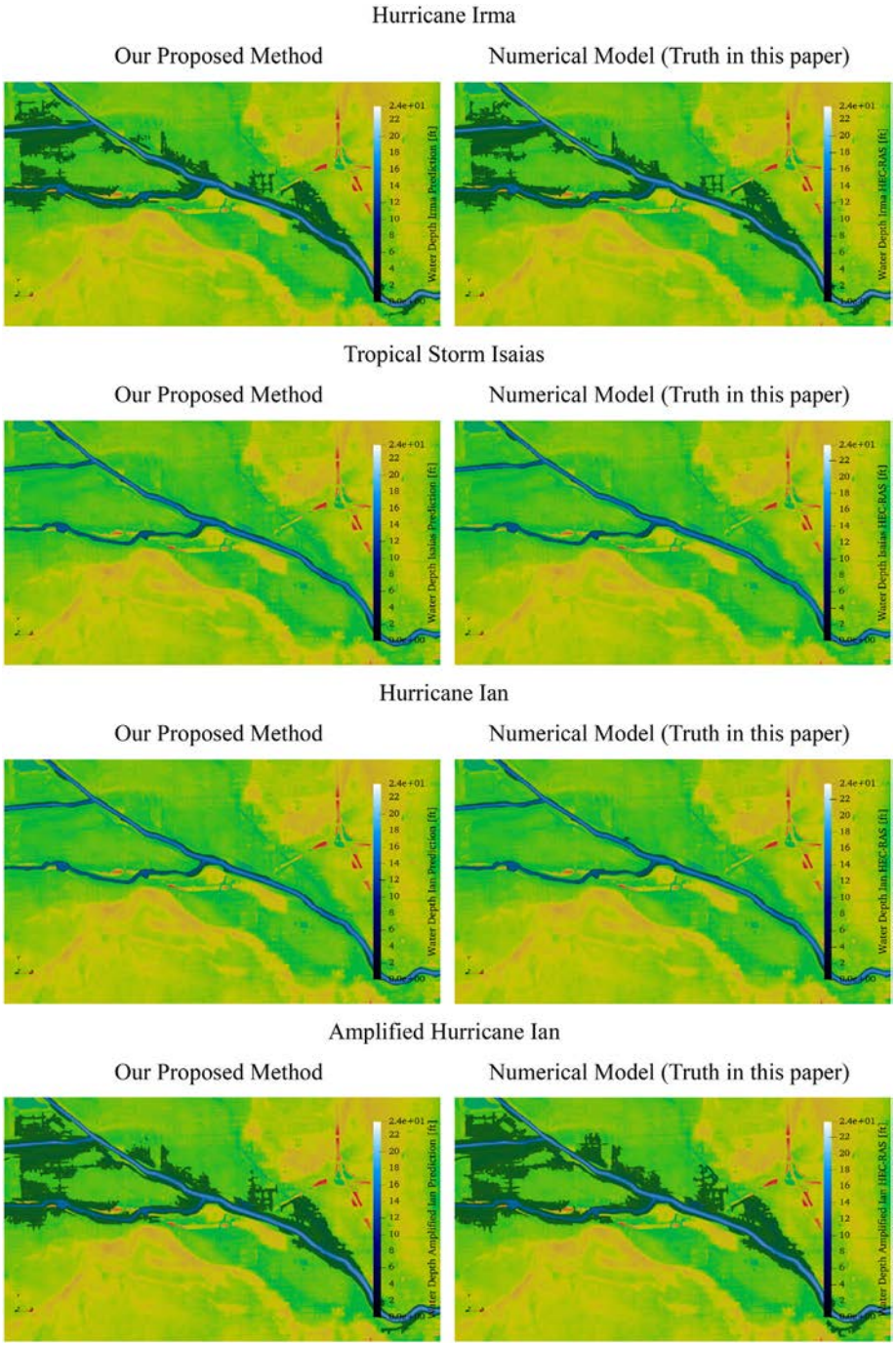

Fig. 6. Predicted water depth (our method) and HEC-RAS simulated water depth (ground truth) at maximum inundation timestep under different hurricane conditions.

provide accurate predictions, as these patterns are not represented in the training dataset. Alternatively, the issue may be also due to the fact that the total inundation area and the severity of the flood during the amplified Ian event surpass the extent covered in the training dataset, effectively transforming the problem into an extrapolation challenge.

4.2. Error metrics

Accuracy, precision, and recall are three commonly used metrics for assessing flood map predictions (Anbarasan et al., 2020). These metrics are derived from the values of true negatives (TN), false positives (FP), true positives (TP), and false negatives (FN). In the context of our flood map prediction, TN represents the total count of cells that were both simulated as covered by water and correctly predicted as covered by water. FP stands for the total count of cells that were simulated as not covered but were incorrectly predicted as covered by water. FN denotes the total count of cells that were simulated as covered by water but were incorrectly predicted as not covered by water. Lastly, TP value means the total count of cells that were simulated as not covered by water areas and were correctly predicted as not covered by water. The values of these four basic metrics for our proposed method under four test events are depicted in Fig. 9.

Accuracy is used as an error metric to evaluate the correctness of flood detection and can be represented by Eq. 6. Precision, on the other hand, is a metric that assesses the accuracy of attributes in the solution concerning the data. Specifically, it is the ratio of correctly

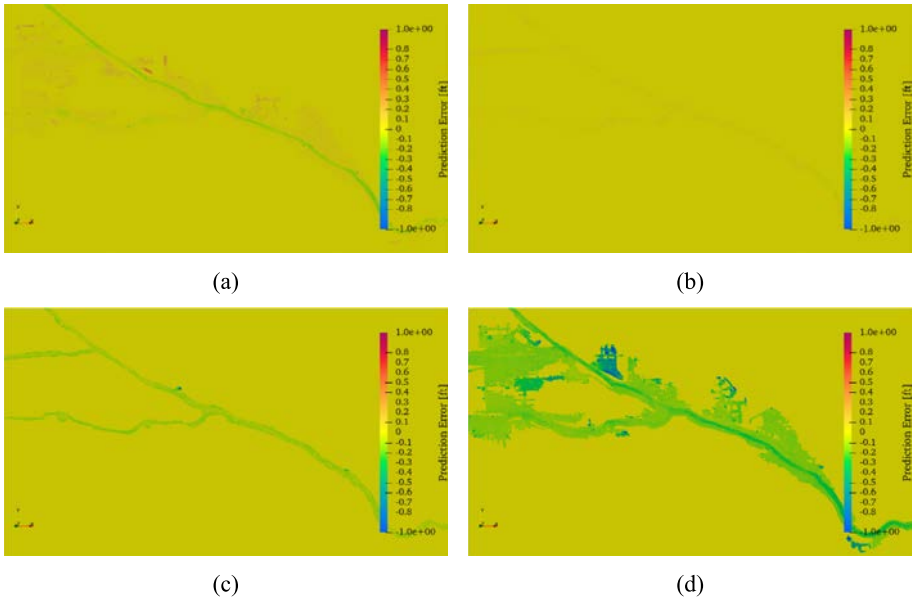

Fig. 7. Prediction error map for different test events: (a) Hurricane Irma; (b) Tropical Storm Isaias; (c) Hurricane Ian; (d) Amplified Hurricane Ian.

predicted flooding cell numbers to the total predicted flooding cell numbers, as defined in Eq. 7. Recall evaluates the effectiveness of the solution from the proposed method in retrieving the correct data attributes. In simpler terms, recall is the ratio of successfully predicted flooding cell numbers to the total flooding cell numbers, calculated using Eq. 8. Critical success index (CSI) is used to measure the accuracy of forecasts and the value of warnings, which is calculated using Eq. 9. The F1 score (as shown in Eq. 10) is calculated as the harmonic mean of precision and recall, providing a balanced representation of both metrics in a single, unified measure. Additionally, as our proposed method

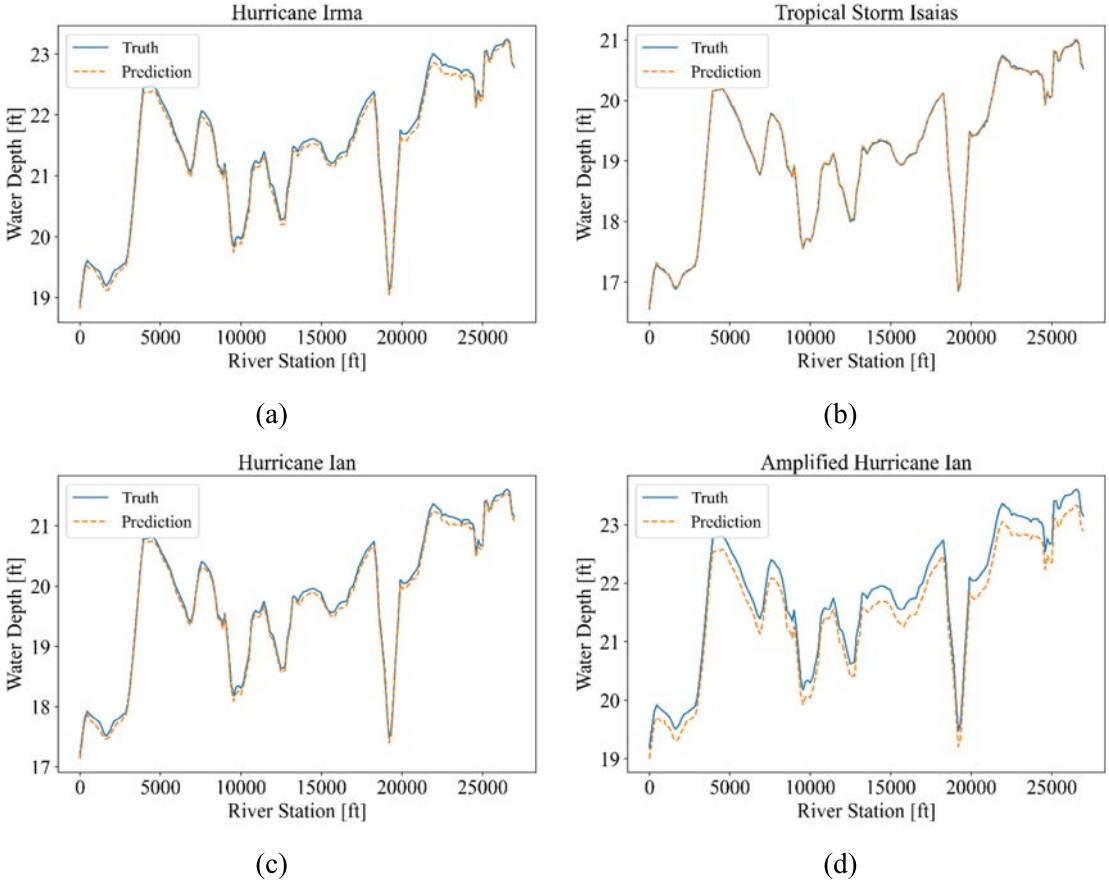

Fig. 8. Predicted water depth and HEC-RAS simulated water depth (ground truth) along the main river channel at maximum flood map: (a) Hurricane Irma; (b) Tropical Storm Isaias; (c) Hurricane Ian; (d) Amplified Hurricane Ian.

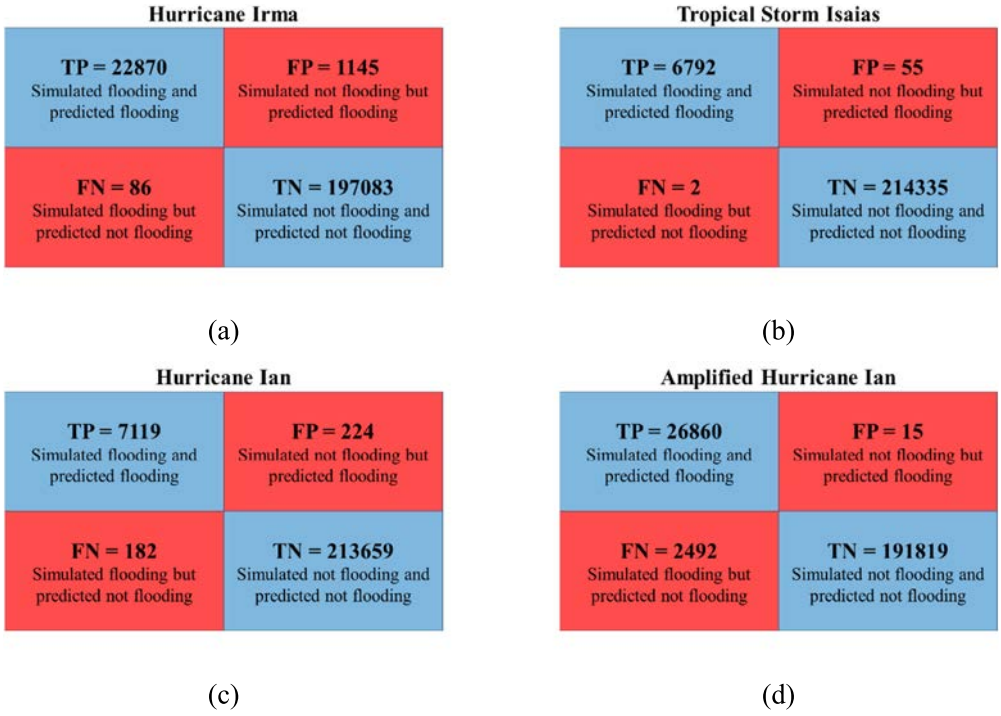

Fig. 9. True positives (TP), false positives (FP), false negatives (FN), and true negative (TN) values for four different test cases: (a) Hurricane Irma; (b) Tropical Storm Isaias; (c) Hurricane Ian; (d) Amplified Hurricane Ian.

provides water depth in each cell rather than a Boolean value in previous research (Bui et al., 2020; Nemni et al., 2020; Muñoz et al., 2021), we can implement other commonly used error metrics to measure accuracy. Mean Absolute Error (MAE, shown in Eq. 11) and Root Mean Square Error (RMSE, shown in Eq. 12) are widely utilized for comparing two arrays. MAE calculates the average absolute difference between the elements of the two arrays, while RMSE calculates the square root of the average squared difference between the elements of the two arrays. Additionally, R-squared (R2, shown in Eq. 13) is a well-known parameter that measures the proportion of the variance in one array that is predictable from the other array. Critical success index (CSI)

$$Accuracy = \frac{TP + TN}{TP + FP + FN + TN} \tag{6}$$

$$Precision = \frac{TP}{TP + FP} \tag{7}$$

$$Recall = \frac{TP}{TP + FN} \tag{8}$$

$$CSI = \frac{TP}{TP + FP + FN} \tag{9}$$

$$F1 = \frac{2 * TP}{2 * TP + FP + FN} \tag{10}$$

$$MAE = \frac{\sum_{i=1}^{n} \left(Y_{prediction} - Y_{true}\right)}{n} \tag{11}$$

$$RMSE = \sqrt{\frac{\sum_{i=1}^{n} \left(Y_{prediction} - Y_{true}\right)^2}{n}} \tag{12}$$

$$R^2 = 1 - \frac{\sum_{i=1}^{n} \left(Y_{prediction} - Y_{true}\right)^2}{\sum_{i=1}^{n} \left(Y_{prediction} - \overline{Y_{prediction}}\right)^2} \tag{13}$$

where $Y_{prediction}$ represents the proposed model output, $\overline{Y_{prediction}}$ stands for the mean value of the model outputs, Y_{true} represents ground truth, $\overline{Y_{true}}$ stands for the mean value of the ground truth, and n means the number of total sample points.

Table 1 summarizes the aforementioned performance metrics for our proposed method across the four test scenarios. Overall, the six

Table 1
Performance metrics of proposed method under test cases.

	Hurricane Irma	Tropical Storm Isaias	Hurricane Ian	Amplified Hurricane Ian
Accuracy	0.99443	0.99974	0.99816	0.98867
Precision	0.95232	0.99197	0.96949	0.99944
Recall	0.99625	0.99971	0.97507	0.91510
CSI	0.94892	0.99168	0.94605	0.91463
F1	0.97379	0.99582	0.97228	0.95541
MAE [ft]	0.00498	0.00072	0.00282	0.02475
RMSE [ft]	0.02194	0.00523	0.01789	0.08261
R2	0.99994	0.99999	0.99995	0.99919

Table 2
Parametric study of transformer encoder layer.

	0 layer	1 layer	4 layers	8 layers
MAE [ft]	0.01389	0.01220	0.00717	0.01011
RMSE [ft]	0.07821	0.06444	0.03974	0.05634

metrics indicate strong alignment with the ground truth data, as values of 0.9 are generally considered a good threshold for accuracy, precision, and recall, while a threshold of 0.7 is typically regarded as good for the CSI and F1 score. The test case of Tropical Storm Isaias shows the best performance because there is no overland flood involved so that makes it a relatively simpler condition. As the area of overland flooding increases, all performance metrics are observed tend to decrease, indicating overland flood prediction is still a very challenging issue, as illustrated in Figs. 6 and 7. Notably, the precision value is lower than other metrics in the Hurricane Irma event, suggesting that our proposed method tends to over-predict the flood area under this scenario. Conversely, in the Amplified Hurricane Ian event, the recall value is significantly lower than the others, indicating an overall underestimation of the total flood area. The prediction for the Hurricane Ian case holds a general balance between overestimation and underestimation. The Amplified Hurricane Ian test case exhibits the worst metric indexes in MAE, RMSE, and R2, indicating larger prediction errors compared to the other test cases. This observation aligns with the visual errors depicted in Fig. 6 and Fig. 7. The larger prediction errors observed in the amplified Hurricane Ian test case imply a potential need for enrichment of heavy flooding training cases.

4.3. Model architecture study

The Transformer encoder is designed to transform tabulated time series data into a 2D feature map, and then the U-Net structure processes the 2D feature map along with geophysical data to make the final prediction. Both components offer flexibility in determining the depth of higher-level features. In the Transformer encoder, the multi-head self-attention and MLP block are typically repeated multiple times, as denoted by $N\times$ in Fig. 2, to achieve optimal performance. Therefore, we conducted a parametric study to determine the number of layers needed to achieve the best performance, and the results are shown in Table 2. In this section, we compute error metrics based on the entire test set to streamline the paper. Consequently, some metrics, such as accuracy, precision, recall, and R2, may no longer be suitable for the combined dataset.

In Table 2, "0 layers" indicate the absence of Transformer encoder layers in our designed model, resulting in the highest error. As the number of Transformer encoder layers increases to 4, the proposed model achieved its optimal performance in our dataset. The MAE and RMSE remain relatively low even without the Transformer encoder layers, mainly because most data points fall under the TN category in Fig. 9, meaning the majority of pixels have zero water depth. As a result, the model's performance without Transformer encoder layers may appear worse than the error metrics suggest. In such case, small increases in error are more significant than they may intuitively seem. The Transformer encoder layers can reduce the error by half, highlighting their critical role in improving the model's understanding of time-series data and generating a more effective feature map for the subsequent U-Net processing. In previous computer vision studies (Dosovitskiy et al., 2020; Ding et al., 2021; Dou et al., 2022), employing deeper transformer encoder layers, up to 8 or 12 layers, demonstrated improved performance. However, such performance benefits were not observed in this study. The discrepancy may be due to the fact that those studies trained on very large datasets, typically with over 10 million samples. However, in our flood map case, accessing such a large number of training samples is usually not feasible in practice.

Another key element of our proposed method is the U-Net. There are no established guidelines on how deep the extraction of high-level features should go. Previous research typically extracted features to 4–6 layers with channel counts ranging from 512 to 2048. Therefore, we conducted a parametric study to explore the number of layers that would achieve the best performance. We utilized the optimal transformer encoder layers of 4 as found above for this investigation. The results of the parametric study on U-Net depth are presented in Table 3. The model performs better as the number of layers increases, reaching its optimal performance at 5 layers (1024 channels) in our dataset. This suggests that extracting higher-level features indeed contributes to improved model performance. The potential reason for the sharp performance drop when the number of layers increases to 6 is that highest level features map may become too small. Since the original resolution of our flood map is 576×384, the highest-level feature map resolution after 6 layers of condensing would be reduced to 18×12. Extracting a medium-resolution map into a total of 216 elements may lead to the issue of over-extraction.

In our proposed method, three feature maps, elevation, slope, and Manning's coefficient, were integrated with processed boundary conditions before entering the U-Net. These three features remain constant and do not change with boundary conditions or events throughout all training and test datasets. However, as indicated by Eq. 5, these features are crucial for predicting the flood map. Thus, we conducted a test on feature reduction to assess the model's performance with a reduced universal feature map. The results of this study are presented in Table 4.

As Table 4 shows, the model's performance declined when the slope information was removed. However, when either elevation or Manning's coefficient information was removed, the learning curve initially dropped, but it soon plateaued. The output essentially converged to the mean value everywhere, indicating that the model struggled to

Table 3
Parametric study of U-Net depth.

	3 layer (up to 256 channels)	4 layer (up to 512 channels)	5 layer (up to 1024 channels)	6 layer (up to 2048 channels)
MAE [ft]	0.01129	0.00837	0.00717	0.01818
RMSE [ft]	0.061922	0.04405	0.03974	0.091037

Table 4
Coupled feature number study.

	Only Manning's coefficient	Only elevation	Elevation and Manning's	All features
MAE [ft]	Not learnable	Cannot converge	0.02132	0.00717
RSME [ft]	Not learnable	Cannot converge	0.10062	0.03974

learn complex patterns without sufficient assistance from geophysical information. In the absence of elevation or Manning's coefficient information, the model struggled to optimize, and the loss remained at a persistently high initial value. Thus, while slope information contributes to the model's understanding of the dataset, elevation and roughness information are crucial for the model's regression capabilities. This conclusion also matches the information from Eq. 5 as well.

A notable observation based on this entire parametric study section is that altering the model architecture often leads to only slight modifications in performance, whereas selecting or providing enough essential physical information tends to have a much more significant impact on machine learning models.

5. Discussion

5.1. Benefits and drawbacks of using our proposed method

The primary advantage of our proposed approach lies in its capability to integrate speed and high accuracy. With our method, when dealing with the 7-day rainfall event, obtaining the maximum flood map takes only 5 s when using Nvidia RTX 4070, whereas running a high-fidelity full-momentum HEC-RAS model averages around 3 h when using AMD Ryzen 5090×. This significant reduction in computation time can have a significant impact on decision-making and execution stage during large stormwater events. In the context of flood emergency evacuations, where every second matters, this fast prediction could provide huge value. Another area where a rapid response is highly beneficial is flow optimization problems. Traditionally, researchers and engineers have to use 1D models as response surfaces, predictive models, or environments to integrate with optimization algorithms due to the large time requirements of 2D models. Most optimization algorithms typically require running the response surface or predictive model thousands of times to obtain the optimal results. However, running a 2D model once can take hours, making the entire optimization process significantly less valuable in practical problems. Although using 1D model are generally faster, they face challenges in accurately providing overland flood information since both sides of the cross-section are typically treated as walls in the numerical solvers. Our proposed method can address this issue, making flow optimization on a 2D predictive model feasible.

Another benefit of our proposed model is its simplicity in usage. In traditional numerical methods, researchers and engineers are required to generate the mesh, considering many factors such as the Courant number, mesh refinement, numerical scheme, and instability. Conducting a correct high-fidelity simulation often demands modelers to have a certain amount of background knowledge in numerical methods, mathematics, and physics. As a regression model, our proposed methods are much more user-friendly, particularly for individuals without extensive knowledge of mathematics.

However, our proposed method has certain limitations and drawbacks compared to conventional methods, as shown in Table 5. Besides, the advantages, a key limitation or drawback of our proposed method is that it is designed specifically for predicting maximum flood hazard maps and cannot compute other important flood information, such as peak discharge, flood wave arrival time, and time to peak flood. Fortunately, this limitation can be easily addressed even within the same framework we proposed. By generating time series map information (a three-dimensional temporal-spatial map) and using it as training output data, we can create a series of maps that resemble a video like information, enabling access to this important flood information. However, this approach will require a GPU with larger memory. Given the limitations of our available hardware, we are unable to fully realize this goal. We strongly recommend that future research explore this direction further. To address this issue, we believe that developing dedicated deep learning models for each key metric (flood wave arrival time, and time to peak flood) might be a practical compromise for practitioners.

Table 5
Pros and Cons comparison between our method and numerical methods.

	Our proposed method	Numerical methods
Computation Speed	<10 s	~3 h
User-friendly	Minimal background knowledge required	Require certain background and engineering knowledge
Scalable	Yes	Yes
Other flood information (e.g. Flood Wave Arrival Time; Time to Peak Flood)	Not supported yet	Can access

5.2. Is it necessary for the computational domain to be rectangular?

The short answer is partially yes. The only supporting shape for the domain of interest is rectangular since the Convolutional Neural Network (CNN) inside our U-Net Residual Block, can only operate within a rectangular shape. However, this does not imply that the watershed or catchment domain must be rectangular, nor does it mean that the boundary of the domain of interest needs to be predetermined. As shown in Fig. 10, the shape of the watershed or catchment can take any irregular shape, and the boundary conditions are positioned at the edge of this irregular shape. Many pervious research have proved that water depth and flow rate in any cross-sections can be trained and inferred as non-flooding 1D scenarios using neural networks (Kabir et al., 2020; Nguyen, 2020; Pan et al., 2020; Ahmed et al., 2022; Castangia et al., 2023; Shi et al., 2023). Similarly, in our scenario, I1, I2, I3, and O1 can be auto-regressed as internal variables based on the watershed boundary, upstream boundaries 1, 2, 3, and downstream boundary, respectively. In this case, Eq. 5 still holds as the boundary at the domain of interest can be internally inferred by the watershed boundary in neural network model. Thus, the proposed method could handle almost all types of watersheds and catchments. In the case study presented in this paper, the catchment is also in an irregular shape, yet accurate predictions are still achieved since our domain of interest is a rectangular shape.

5.3. Limitations of this work

There are two major limitations found in this study. Firstly, our neural network model heavily relies on GPU memory. In our proposed method, the GPU memory requirements depend on the resolution of the target flood map, which is somewhat equal to the total grid number in the numerical method. The resolution of our case study is 576 × 384, equivalent to approximately 221 thousand grid points. This resolution is still trainable for almost all types of GPUs. However, after testing larger resolutions, we discovered that an 8GB GPU memory can only handle up to roughly 300–400 thousand pixels (computational grids) in the training phase. Thus, applying our proposed method to train and predict very large watersheds at high resolution could be challenging due to hardware limitations. Handling such large cases would require one or more industrial-level GPUs to manage the computational demands effectively.

Secondly, our proposed method falls into the category of a “small model” in the definition of machine learning. This implies that one model only works for a specific domain, and retraining is necessary if we want to predict another domain. Although our method may have potential to function as a “large general model,” we are unable to test and prove this because the massive amount of data is usually required for training larger models, which we currently lack the ability to collect. How to generate our model to a universal model could be a good topic for the future research.

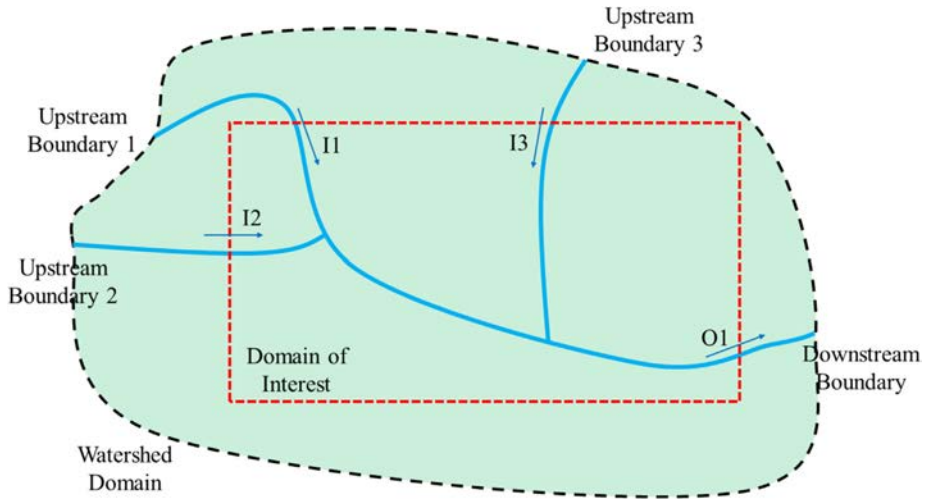

Fig. 10. Illustration of watershed boundary and domain of interest boundary.

6. Conclusion

This paper presents a framework for the direct, rapid, and accurate prediction of riverine flood maps based on given boundary conditions. Predicting flood hazard maps with detailed water levels for each geographical pixel represents a significant advancement, as it offers more valuable insights for practitioners compared to previous studies focused on flood susceptibility maps. Our approach requires minimal training data and can perform accurately even with a small dataset, producing high-resolution flood maps with depth information in approximately 5 s, as opposed to the roughly 3 h required by traditional numerical methods. This drastic reduction in computational time offers significant advantages for flood emergency evacuations and flow optimization problems. The model's performance has also been thoroughly evaluated, demonstrating high accuracy. The key findings are summarized as follows:

- Our approach can accurately predict water depth in both the channel and overland flood areas. The mean absolute errors range from 0.00072 to 0.02475 ft, while the root mean square errors range from 0.00523 to 0.08261 ft. Additionally, the other three metrics, accuracy, precision, and recall, also proved the performance of our proposed model.
- Upon testing hyperparameters in our model, we found that using 4 layers of transformer encoder and 5 layers of U-Net can provide the best performance for our study area.
- Choosing or providing sufficient physical input information has a much more significant impact than altering the model architecture in our riverine flooding prediction problem.

Open research

All AI codes, script code and all data can be found at [https://github.com/ZedaYin/Riverine-Flood-Hazard-Map-Prediction-by-Neural-Networks] for better demonstration and will be permanently available when the article is eventually accepted. Partial data on which this article used for modeling are available in Yin et al. (2024).

CRediT authorship contribution statement

Zeda Yin: Writing – review & editing, Writing – original draft, Visualization, Validation, Methodology, Investigation, Formal analysis, Data curation, Conceptualization. **Arturo S. Leon:** Writing – review & editing, Supervision, Funding acquisition.

Declaration of competing interest

The authors declare that they have no known competing financial interests or personal relationships that could have appeared to influence the work reported in this paper.

Acknowledgement

The authors gratefully acknowledge the financial support from the National Science Foundation under Grant CBET 2203292. Also, the authors are grateful to the anonymous reviewers for their constructive comments, which helped to significantly improve the quality of the manuscript.

References

Ahmed, A.M., Deo, R.C., Ghahramani, A., Feng, Q., Raj, N., Yin, Z., Yang, L., 2022. New double decomposition deep learning methods for river water level forecasting. Sci. Total Environ. 831, 154722.
Amiri, A., Soltani, K., Ebtehaj, I., Bonakdari, H., 2024. A novel machine learning tool for current and future flood susceptibility mapping by integrating remote sensing and geographic information systems. J. Hydrol. 632, 130936.
Anbarasan, M., Muthu, B., Sivaparthipan, C.B., Sundarasekar, R., Kadry, S., Krishnamoorthy, S., Dasel, A.A., 2020. Detection of flood disaster system based on IoT, big data and convolutional deep neural network. Comput Commun 150, 150–157.
Azzi, Z., Matus, M., Elawady, A., Zisis, I., Irwin, P., Gan Chowdhury, A., 2020. Aeroelastic testing of span-wire traffic signal systems. Frontiers in Built Environment 6, 111.
Bentivoglio, R., Isufi, E., Jonkman, S.N., Taormina, R., 2022. Deep learning methods for flood mapping: a review of existing applications and future research directions. Hydrol. Earth Syst. Sci. 26 (16), 4345–4378.
Berkhahn, S., Fuchs, L., Neuweiler, I., 2019. An ensemble neural network model for real-time prediction of urban floods. J. Hydrol. 575, 743–754.
Bevacqua, E., Maraun, D., Vousdoukas, M.I., Voukouvalas, E., Vrac, M., Mentaschi, L., Widmann, M., 2019. Higher probability of compound flooding from precipitation and storm surge in Europe under anthropogenic climate change. Sci. Adv. 5 (9), eaaw5531.
Bui, D.T., Hoang, N.D., Martínez-Álvarez, F., Ngo, P.T.T., Hoa, P.V., Pham, T.D., et al., 2020. A novel deep learning neural network approach for predicting flash flood susceptibility: a case study at a high frequency tropical storm area. Sci. Total Environ. 701, 134413.
Castangia, M., Grajales, L.M.M., Aliberti, A., Rossi, C., Macii, A., Macii, E., Patti, E., 2023. Transformer neural networks for interpretable flood forecasting. Environ. Model. Software 160, 105581.
Chang, H., Zhang, H., Barber, J., Maschinot, A.J., Lezama, J., Jiang, L., et al., 2023. Muse: Text-to-image generation via masked generative transformers. arXiv preprint arXiv: 2301.00704.
Chen, J., Shi, X., Gu, L., Wu, G., Su, T., Wang, H.M., et al., 2023. Impacts of climate warming on global floods and their implication to current flood defense standards. J. Hydrol. 618, 129236.
Cred, U., 2018. Economic Losses, Poverty & Disasters 1998–2017. Université Catholique de Louvain (UCL), Brussels, Belgium, p. 33.
Ding, M., Yang, Z., Hong, W., Zheng, W., Zhou, C., Yin, D., et al., 2021. Cogview: mastering text-to-image generation via transformers. Advances in Neural Information Processing Systems 34, 19822–19835.

Dosovitskiy, A., Beyer, L., Kolesnikov, A., Weissenborn, D., Zhai, X., Unterthiner, T., et al., 2020. An image is worth 16x16 words: Transformers for image recognition at scale. arXiv preprint arXiv:2010.11929.
Dou, Z.Y., Xu, Y., Gan, Z., Wang, J., Wang, S., Wang, L., et al., 2022. An empirical study of training end-to-end vision-and-language transformers. Proceedings of the IEEE/CVF Conference on Computer Vision and Pattern Recognition, pp. 18166–18176.
Esfandiari, M., Abdi, G., Jabari, S., McGrath, H., Coleman, D., 2020. Flood hazard risk mapping using a pseudo supervised random forest. Remote Sens. (Basel) 12 (19), 3206.
Farhadi, H., Najafzadeh, M., 2021. Flood risk mapping by remote sensing data and random forest technique. Water 13 (21), 3115.
Fereshtehpour, M., Esmaeilzadeh, M., Alipour, R.S., Burian, S.J., 2024. Impacts of DEM type and resolution on deep learning-based flood inundation mapping. Earth Sci. Inf. 17 (2), 1125–1145.
FLO-2D, 2018. FLO-2D Pro version: Two-Dimensional flood Routing Model.
Fraehr, N., Wang, Q.J., Wu, W., Nathan, R., 2023. Supercharging hydrodynamic inundation models for instant flood insight. Nature Water 1–9.
Gu, L., Chen, J., Yin, J., Slater, L.J., Wang, H.M., Guo, Q., et al., 2022. Global increases in compound flood-hot extreme hazards under climate warming. Geophys. Res. Lett. 49 (8) e2022GL097726.
Ha, S., Liu, D., Mu, L., 2021. Prediction of Yangtze River streamflow based on deep learning neural network with El Niño–Southern Oscillation. Sci. Rep. 11 (1), 11738.
Haltas, I., Yildirim, E., Oztas, F., Demir, I., 2021. A comprehensive flood event specification and inventory: 1930–2020 Turkey case study. International Journal of Disaster Risk Reduction 56, 102086.
He, K., Zhang, X., Ren, S., Sun, J., 2016. Deep residual learning for image recognition. Proceedings of the IEEE Conference on Computer Vision and Pattern Recognition, pp. 770–778.
He, J., Zhang, L., Xiao, T., Wang, H., Luo, H., 2023. Deep learning enables super-resolution hydrodynamic flooding process modeling under spatiotemporally varying rainstorms. Water Res. 239, 120057.
Hitouri, S., Mohajane, M., Lahsaini, M., Ali, S.A., Setargie, T.A., Tripathi, G., et al., 2024. Flood susceptibility mapping using SAR data and machine learning algorithms in a small watershed in northwestern Morocco. Remote Sens. (Basel) 16 (5), 858.
Hosseiny, H., 2021. A deep learning model for predicting river flood depth and extent. Environ. Model. Software 145, 105186.
Hosseiny, H., Nazari, F., Smith, V., Nataraj, C., 2020. A framework for modeling flood depth using a hybrid of hydraulics and machine learning. Sci. Rep. 10 (1), 8222.
Kabir, S., Patidar, S., Xia, X., Liang, Q., Neal, J., Pender, G., 2020. A deep convolutional neural network model for rapid prediction of fluvial flood inundation. J. Hydrol. 590, 125481.
Kabir, S., Patidar, S., Pender, G., 2021, February. A machine learning approach for forecasting and visualising flood inundation information. Proceedings of the Institution of Civil Engineers-Water Management. vol. 174. Thomas Telford Ltd., pp. 27–41 No. 1.
Kam, P.M., Aznar-Siguan, G., Schewe, J., Milano, L., Ginnetti, J., Willner, S., et al., 2021. Global warming and population change both heighten future risk of human displacement due to river floods. Environ. Res. Lett. 16 (4), 044026.
Kim, H.I., Han, K.Y., 2020. Urban flood prediction using deep neural network with data augmentation. Water 12 (3), 899.
Kousky, C., Palim, M., Pan, Y., 2020. Flood damage and mortgage credit risk: a case study of hurricane Harvey. J. Hous. Res. 29 (sup1), S86–S120.
Lai, Y.G., 2010. Two-dimensional depth-averaged flow modeling with an unstructured hybrid mesh. J. Hydraul. Eng. 136 (1), 12–23.
Liao, Y., Wang, Z., Lai, C., Xu, C.Y., 2023. A framework on fast mapping of urban flood based on a multi-objective random Forest model. Int. J. Disaster Risk Sci. 1–16.
Liu, Z., Lin, Y., Cao, Y., Hu, H., Wei, Y., Zhang, Z., et al., 2021. Swin transformer: Hierarchical vision transformer using shifted windows. Proceedings of the IEEE/CVF International Conference on Computer Vision, pp. 10012–10022.
Liu, Y., Hu, T., Zhang, H., Wu, H., Wang, S., Ma, L., Long, M., 2023. Itransformer: inverted transformers are effective for time series forecasting. arXiv preprint arXiv: 2310.06625.
Löwe, R., Böhm, J., Jensen, D.G., Leandro, J., Rasmussen, S.H., 2021. U-FLOOD–topographic deep learning for predicting urban pluvial flood water depth. J. Hydrol. 603, 126898.
Martínez-Aranda, S., Fernández-Pato, J., Echeverribar, I., Navas-Montilla, A., Morales-Hernández, M., Brufau, P., et al., 2022. Finite volume models and efficient simulation tools (EST) for shallow flows. Advances in Fluid Mechanics: Modelling and Simulations. Springer Nature Singapore, Singapore, pp. 67–137.
Muñoz, D.F., Muñoz, P., Moftakhari, H., Moradkhani, H., 2021. From local to regional compound flood mapping with deep learning and data fusion techniques. Sci. Total Environ. 782, 146927.
Nemni, E., Bullock, J., Belabbes, S., Bromley, L., 2020. Fully convolutional neural network for rapid flood segmentation in synthetic aperture radar imagery. Remote Sens. (Basel) 12 (16), 2532.
Nguyen, X.H., 2020. Combining statistical machine learning models with ARIMA for water level forecasting: the case of the red river. Adv. Water Resour. 142, 103656.
NOAA, 2016. U.S. Climate Resilience Toolkit. Inland Flooding URL https://toolkit.climate.gov/topics/coastal-flood-risk/inland-flooding.
Ongdas, N., Akiyanova, F., Karakulov, Y., Muratbayeva, A., Zinabdin, N., 2020. Application of HEC-RAS (2D) for flood hazard maps generation for Yesil (Ishim) river in Kazakhstan. Water 12 (10), 2672.
Pan, M., Zhou, H., Cao, J., Liu, Y., Hao, J., Li, S., Chen, C.H., 2020. Water level prediction model based on GRU and CNN. Ieee Access 8, 60090–60100.
Parhi, P.K., 2018. Flood management in Mahanadi Basin using HEC-RAS and Gumbel's extreme value distribution. Journal of The Institution of Engineers (India): Series A 99 (4), 751–755 550.
Park, K., Jung, Y., Seong, Y., Lee, S., 2022. Development of deep learning models to improve the accuracy of water levels time series prediction through multivariate hydrological data. Water 14 (3), 469.
Pathan, A.I., Agnihotri, P.G., Patel, D., Prieto, C., 2022. Mesh grid stability and its impact on flood inundation through (2D) hydrodynamic HEC-RAS model with special use of big data platform—a study on Purna River of Navsari city. Arab. J. Geosci. 15 (7), 659.
Rahman, M., Chen, N., Islam, M.M., Mahmud, G.I., Pourghasemi, H.R., Alam, M., et al., 2021. Development of flood hazard map and emergency relief operation system using hydrodynamic modeling and machine learning algorithm. J. Clean. Prod. 311, 127594.
Ronneberger, O., Fischer, P., Brox, T., 2015. U-net: convolutional networks for biomedical image segmentation. Medical image computing and computer-assisted intervention–MICCAI 2015: 18th international conference, Munich, Germany, October 5-9, 2015, proceedings, part III. 18. Springer International Publishing, pp. 234–241.
Ruiz, N., Li, Y., Jampani, V., Pritch, Y., Rubinstein, M., Aberman, K., 2023. Dreambooth: fine tuning text-to-image diffusion models for subject-driven generation. Proceedings of the IEEE/CVF Conference on Computer Vision and Pattern Recognition, pp. 22500–22510.
Saharia, C., Chan, W., Saxena, S., Li, L., Whang, J., Denton, E.L., Norouzi, M., 2022. Photorealistic text-to-image diffusion models with deep language understanding. Adv. Neural Inf. Proces. Syst. 35, 36479–36494.
Seydi, S.T., Kanani-Sadat, Y., Hasanlou, M., Sahraei, R., Chanussot, J., Amani, M., 2022. Comparison of machine learning algorithms for flood susceptibility mapping. Remote Sens. (Basel) 15 (1), 192.
Shaikh, A.A., Pathan, A.I., Waikhom, S.I., Agnihotri, P.G., Islam, M.N., Singh, S.K., 2023. Application of latest HEC-RAS version 6 for 2D hydrodynamic modeling through GIS framework: a case study from coastal urban floodplain in India. Modeling Earth Systems and Environment 9 (1), 1369–1385.
Shi, J., Yin, Z., Myana, R., Ishtiaq, K., John, A., Obeysekera, J., et al., 2023. Deep learning models for water stage predictions in south florida. arXiv preprint arXiv:2306.15907.
Tamiru, H., Dinka, M.O., 2021. Application of ANN and HEC-RAS model for flood inundation mapping in lower Baro Akobo River Basin, Ethiopia. Journal of Hydrology: Regional Studies 36, 100855.
Tehrany, M.S., Jones, S., Shabani, F., 2019. Identifying the essential flood conditioning factors for flood prone area mapping using machine learning techniques. Catena 175, 174–192.
USACE, 2018. HEC-RAS River Analysis System (Version 5.0.6).
Vaswani, A., Shazeer, N., Parmar, N., Uszkoreit, J., Jones, L., Gomez, A.N., Polosukhin, I., 2017. Attention is all you need. Adv. Neural Inf. Proces. Syst. 30.
Voosen, P., 2022. Studies tying weather extremes to global warming gain rigor. Science 376 (6599), 1256–1257.
Xie, S., Wu, W., Mooser, S., Wang, Q.J., Nathan, R., Huang, Y., 2021. Artificial neural network based hybrid modeling approach for flood inundation modeling. J. Hydrol. 592, 125605.
Yan, Y., Zhang, W., Liu, Y., Li, Z., 2023. Simulated annealing algorithm optimized GRU neural network for urban rainfall-inundation prediction. Journal of Hydroinformatics 25 (4), 1358–1379.
Yin, Z., Bian, L., Hu, B., Shi, J., Leon, A.S., 2023. Physic-informed neural network approach coupled with boundary conditions for solving 1D steady shallow water equations for riverine system. World Environmental and Water Resources Congress 2023, pp. 280–288.
Yin, Z., Saadati, Y., Hu, B., Leon, A.S., Amini, M.H., McDaniel, D., 2024. Fast high-fidelity flood inundation map generation by super-resolution techniques. J. Hydroinf. 26 (1), 319–336.
Zhou, L., Kang, L., 2023. A comparative analysis of multiple machine learning methods for flood routing in the Yangtze River. Water 15 (8), 1556.